



## Recursive calibration of the fiber response function for spherical deconvolution of diffusion MRI data

Chantal M.W. Tax<sup>a,\*</sup>, Ben Jeurissen<sup>b</sup>, Sjoerd B. Vos<sup>a</sup>, Max A. Viergever<sup>a</sup>, Alexander Leemans<sup>a</sup>

<sup>a</sup> Image Sciences Institute, University Medical Center Utrecht, Utrecht, The Netherlands

<sup>b</sup> iMinds-Vision Lab, Department of Physics, University of Antwerp, Antwerp, Belgium

### ARTICLE INFO

#### Article history:

Accepted 29 July 2013

Available online 5 August 2013

#### Keywords:

Diffusion MRI

Constrained spherical deconvolution

Tractography

Fiber orientation distribution function

Fiber response function

### ABSTRACT

There is accumulating evidence that at current acquisition resolutions for diffusion-weighted (DW) MRI, the vast majority of white matter voxels contains “crossing fibers”, referring to complex fiber configurations in which multiple and distinctly differently oriented fiber populations exist. Spherical deconvolution based techniques are appealing to characterize this DW intra-voxel signal heterogeneity, as they provide a balanced trade-off between constraints on the required hardware performance and acquisition time on the one hand, and the reliability of the reconstructed fiber orientation distribution function (fODF) on the other hand. Recent findings, however, suggest that an inaccurate calibration of the response function (RF), which represents the DW signal profile of a single fiber orientation, can lead to the detection of spurious fODF peaks which, in turn, can have a severe impact on tractography results. Currently, the computation of this RF is either model-based or estimated from selected voxels that have a fractional anisotropy (FA) value above a predefined threshold. For both approaches, however, there are user-defined settings that affect the RF and, consequently, fODF estimation and tractography. Moreover, these settings still rely on the second-rank diffusion tensor, which may not be the appropriate model, especially at high b-values. In this work, we circumvent these issues for RF calibration by excluding “crossing fibers” voxels in a recursive framework. Our approach is evaluated with simulations and applied to in vivo and ex vivo data sets with different acquisition settings. The results demonstrate that with the proposed method the RF can be calibrated in a robust and automated way without needing to define ad-hoc FA threshold settings. Our framework facilitates the use of spherical deconvolution approaches in data sets in which it is not straightforward to define RF settings a priori.

© 2013 Elsevier Inc. All rights reserved.

### Introduction

Diffusion weighted MRI (DW-MRI) allows for non-invasive characterization of brain microstructure and the directional organization of neural fiber tissue in vivo (Basser et al., 1994; Le Bihan and Johansen-Berg, 2012; Le Bihan et al., 1986; Moseley et al., 1990). The signal that is measured with DW-MRI is related to the amount of water diffusion and depends on several properties of the underlying tissue. Descriptive models that relate this signal to diffusion in fibrous tissue can provide markers of microstructural tissue organization. The most commonly used model to obtain such biomarkers is the second-rank diffusion tensor (Basser et al., 1994), which describes the signal adequately in case of aligned axons that hinder the diffusion. Measures derived from diffusion tensor imaging (DTI), like mean diffusivity (MD) and fractional anisotropy (FA), can be modulated by microstructural tissue components, such as myelination and cell membrane density (Beaulieu, 2002), and

have already shown their value in a wide range of applications (Carballedo et al., 2012; De Groof et al., 2009; Langen et al., 2012; Lebel et al., 2008; Scholz et al., 2009; Verhoeven et al., 2012; Wang et al., 2012).

It is well-known that DTI is unable to model multiple fiber populations within one voxel (Alexander et al., 2001; Frank, 2002; Tournier et al., 2011). The amount of white matter (WM) voxels that exhibits such a configuration with multiple fiber populations has recently been estimated to be around 90% (Jeurissen et al., 2013), which makes this a significant problem for the validity of DTI and, consequently, DTI based tractography approaches. Several approaches have been developed to address this issue of multiple fiber directions within a voxel. Techniques such as Q-ball imaging (Descoteaux et al., 2007; Hess et al., 2006; Tuch, 2004) and diffusion spectrum imaging (Wedeen et al., 2005) can reconstruct the diffusion orientation distribution function (dODF) that is related to water diffusion. Another category for dealing with “crossing fibers” consists of the so-called spherical deconvolution (SD) techniques, which attempt to infer information about the fiber orientations themselves (Anderson, 2005; Dell’Acqua et al., 2007; Descoteaux et al., 2009; Tournier et al., 2004). Constrained SD (CSD), one of the more popular SD approaches (Emsell et al., 2013;

\* Corresponding author at: Image Sciences Institute, University Medical Center Utrecht, Room Q.S.459, P.O. Box 85500, 3508 GA, Utrecht, The Netherlands.

E-mail address: [chantal@isi.uu.nl](mailto:chantal@isi.uu.nl) (C.M.W. Tax).

URL: <http://www.isi.uu.nl/People/?chantal> (C.M.W. Tax).

McGrath et al., 2013; Metzler-Baddeley et al., 2012; Reijmer et al., 2012, 2013a, 2013b; Vos et al., 2012), can reconstruct the fiber orientation distribution function (fODF) in a robust way with scanning protocols that can be used in clinical practice (Tournier et al., 2007). The diffusion signal is then modeled by the convolution of the fODF with a kernel that represents the DW signal corresponding to a single fiber orientation. The fODF is then “deconvolved” from the DW signal (hence, spherical deconvolution) using this kernel, coined the response function (RF).

There are several ways to construct the RF. For instance, it can be modeled by an axially symmetric tensor with a given FA and MD (Anderson, 2005; Descoteaux et al., 2009; Tournier et al., 2004), providing a good fit to the DW signal for a single fiber orientation at low b-values. At high b-values, however, the DW signal deviates significantly from the Gaussian distribution, even in single fiber populations (Clark and Le, 2000), due to restricted diffusion components (Assaf et al., 2004). In other work, the RF is estimated (also referred to as the “RF calibration” step) from the DW signals in voxels with FA values that are typically larger than a user-defined threshold (Jeurissen et al., 2011, 2013; Tournier et al., 2007). The reliability of the FA, however, is generally poor for high b-value and low-SNR DW-MRI data (Jones and Basser, 2004). In addition, high FA values can still be present in regions with crossing fibers (e.g., in case of two fiber populations, of which one has a small volume fraction (VF)), violating the assumption that the corresponding DW signals represent the diffusion profile of a single fiber population. Irrespective of these concerns, prior knowledge is required to calibrate the RF for fODF estimation with SD. Fig. 1 illustrates an example of the difference in resulting fODF peak orientations for two different FA thresholds in RF calibration. In this example, there is an angle difference between the main peak orientations. In addition, the fODF with an FA threshold of 0.8 exhibits two peaks, whereas with an FA threshold of 0.7, there is only peak orientation. Although the sensitivity of such user-defined settings is typically considered to be insignificant, recent research by Parker et al. (2013) clearly demonstrates that inaccurate characterization of the RF can produce spurious peaks, angular deviations of fODF peaks, and poor estimations of VFs of the various fiber populations.

In this work, we present a recursive framework to calibrate the RF which avoids the need of any user-defined settings related to DTI. After a coarse initialization of the RF, CSD is performed to identify and, subsequently, exclude voxels that contain multiple fODF peaks. From the remaining voxels the RF is updated and used for the next iteration. This procedure is repeated until only voxels with one fODF peak are left, thus, assuring that the final RF reflects the DW signal for a single fiber orientation. This framework is evaluated with simulated data to

investigate its convergence properties and its robustness with respect to data noise. We also applied the proposed RF calibration approach to (i) conventional in vivo human brain data; (ii) ex vivo human brain data (Miller et al., 2011); and (iii) ex vivo data from the cervical spinal cord of the vervet monkey (Lundell et al., 2011), demonstrating the general applicability of our framework.

## Methods

### fODF estimation using CSD

SD techniques use high angular resolution diffusion imaging (HARDI) sampling schemes to enable an accurate angular characterization of the diffusion signal (Tuch et al., 2002). Typically, a single shell of the q-space is sampled at a higher b-value compared to DTI. The diffusion signal on this shell can then be modeled as the convolution of the RF with an fODF. If the RF is known, the fODF can be found by the deconvolution of the diffusion signals with this RF, a processing step that is generally ill-posed (Tournier et al., 2004). By using regularization, Tournier et al. further improved the SD approach, which is then referred to as *constrained SD*, drastically reducing its sensitivity to noise (Tournier et al., 2007). A maximum harmonic degree of 8 (i.e.,  $L_{\max} = 8$ ) is generally recommended for the spherical harmonics (SH) representations when performing CSD (Tournier et al., 2009). After a succinct description of the conventional way to obtain the RF (see the *Conventional RF calibration* section), we outline our proposed recursive framework for RF calibration in the *Recursive RF calibration* section.

### Conventional RF calibration

In summary, voxels are identified that satisfy a predefined criterion, typically  $FA > 0.7$ , assuming that the corresponding DW signals represent diffusion profiles of a single fiber population. The DW signals in these selected voxels are then reoriented such that the first eigenvector of the diffusion tensor becomes aligned along a particular axis (usually the z-axis). Subsequently, the SH representations of the adjusted DW signals are averaged across these voxels to obtain a reliable estimate for the RF. During this step, only the SH coefficients with  $m = 0$  are estimated (where  $m$  is the order of the SH function), thereby constraining the RF to be an axially symmetric function (Tournier et al., 2007). In the following, we will refer to this conventional way of RF calibration as the “FA method”, given that the shape of the RF will be mainly determined by the FA threshold that is chosen.

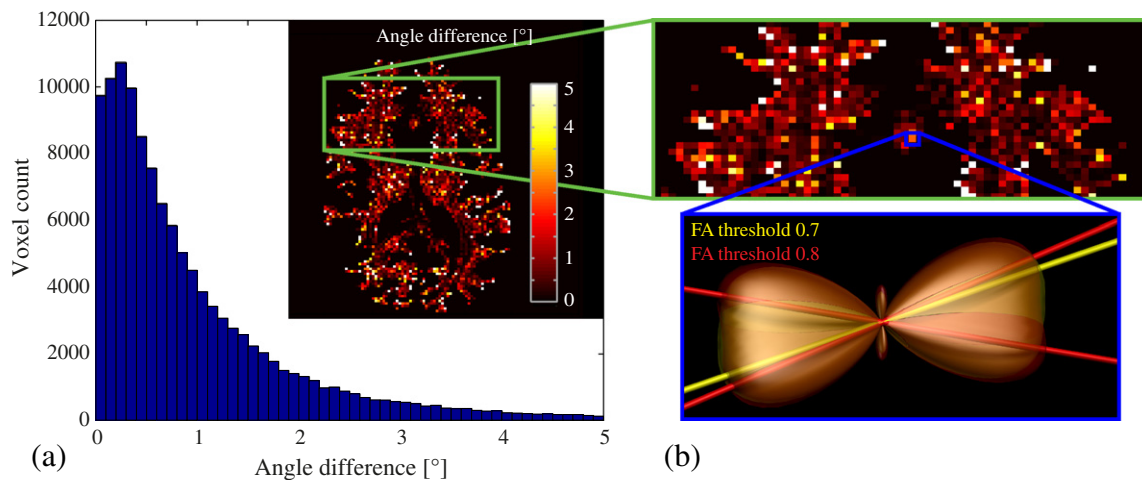


**Fig. 1.** (a) Histogram of the angles between the dominant peaks of the fiber orientation distribution obtained with CSD and with FA thresholds of 0.7 and 0.8 for estimating the response function. The spatial distribution of this angular difference, illustrated for an axial slice, is shown enlarged in the top image in (b). The bottom image in (b) represents the fODF and its peak orientations for both FA thresholds in a single voxel in the corpus callosum. In this example, both the main peak orientations and the number of peaks differ between the two threshold settings.

### Recursive RF calibration

Although there are slight variations in the conventional methodology to calibrate the RF, most approaches to date still rely on properties of the diffusion tensor (i.e., first eigenvector and FA). With the FA being an unreliable measure to differentiate between single and multiple fiber populations, it is desirable to avoid the diffusion tensor model for RF calibration altogether. Therefore, in this work, we propose a recursive framework to compute the RF, consisting of the following steps (for a schematic overview, see Fig. 2):

- 1) Initialize the RF with a diffusion profile shape that is significantly less sharp than that of the expected (i.e., “true”) RF. With some abuse of terminology, this initial RF will be referred to as a *fat* RF. In practice, such a coarse initialization of the RF can be easily achieved by taking DW signal profiles that correspond to a near-isotropic diffusion tensor ( $FA = 0.05$ ). The only requirement at this stage is that this fat RF should still exhibit a dominant orientation, as CSD will produce degenerate fODFs otherwise.
- 2) For voxels that were selected from the previous iteration, calculate the fODF using CSD with the RF from the previous iteration. Obviously, if this is the first iteration, then the fat RF initialization from the previous step will be used and the selected voxels could be the entire brain parenchyma or could be constrained to a WM mask (e.g., derived from a  $T_1$  image) to shorten computation time.
- 3) Calculate the direction and magnitude of the fODF peaks using a Newton optimization algorithm (Jeurissen et al., 2011).
- 4) Select the voxels for which the second largest fODF peak is absent or sufficiently small (e.g., below the noise level) compared to the largest fODF peak. In other words, if the ratio of the second largest fODF peak magnitude to the largest fODF peak magnitude (in the following, this will be called the peak ratio – PR) drops below a specific PR threshold, the voxel will be assumed to contain only one genuine fODF peak and, therefore, will be included for RF estimation in the next iteration. Note that this PR threshold represents an elegant user-defined parameter for balancing between sensitivity and specificity given a specific noise level. For instance, if the PR threshold is chosen too small, noisy fODF peaks will be detected as being sufficiently large. As a result, voxels are excluded erroneously for computation of the RF in the next iteration (false-negatives). If, on the other hand, the PR threshold is set too high, voxels with multiple fODF peaks will be included in the next iteration (false-positives).
- 5) Reorient the DW signals in the voxels obtained in step 4) according to their main fiber direction, that is, the largest fODF peak.
- 6) Calculate the new RF from the SH representations of the reoriented DW signals obtained from step 5) and constrain it to be axially symmetric. Continue with step 2) unless one of the following convergence criteria is met: (i) the maximum number of iterations is reached (set to 20, although the algorithm typically converged in nine iterations) or (ii) the RF shape did not change significantly compared to the previous iteration (e.g., less than 1% size difference for each of the SH coefficients).

Note that by using an RF that is fatter than the true RF when performing CSD, the number of fODF peaks will be underestimated, providing an overestimation of the number of voxels containing only one dominant fiber orientation. As such, for a given PR threshold, convergence of the RF computation is always guaranteed. In the remainder of this manuscript, we will refer to our proposed approach as the “recursive method”.

### Simulations

Noise free DW data were generated assuming axially symmetric diffusion tensor profiles for each fiber population ( $MD = 0.7 \cdot 10^{-3} \text{ mm}^2/\text{s}$ ) (Leemans et al., 2005), using a typical 60 direction sampling scheme (Jones et al., 1999) and b-value of  $2500 \text{ s}/\text{mm}^2$ . Three types of simulation data sets were generated to investigate (i) the occurrence of spurious peaks in single fiber simulations and the influence that PR threshold settings would have, (ii) the influence of fiber configuration on convergence of the recursive method, and (iii) the effect of the PR/FA threshold and SNR on the performance of the recursive/FA method. Details of these simulations are provided in the following sections.

#### Simulation data set (i)

In recent work by Parker et al. (2013), simulations have shown that spurious peaks may also occur for single fiber populations. Such simulations can be used to investigate the optimal PR threshold required in step 4) of the recursive RF calibration, to avoid wrong exclusion of true one-fiber voxels. In line with the parameters defined in Parker et al. (2013), we constructed the following simulation data set. A single fiber population aligned with the z-axis is defined, with varying FA values ranging from 0.1 to 0.9 (with steps of 0.1). Noisy data sets (using the Rician data distribution) are generated with SNR of 10, 15, 22, and 30 (defined on the non-DW signal), with 500 noisy realizations each. The resulting signal was deconvolved with an RF, also simulated as a tensor with chosen FA (same ranges). Peaks were extracted and the magnitude of the second peak was calculated as a fraction of the first peak's magnitude. The purpose of this simulated data set is to investigate the relative magnitude of spurious secondary peaks with respect to the main fODF peak for these parameter settings. Ideally, only the voxels containing a single fiber population should be selected for RF calibration.

#### Simulation data set (ii)

The second simulation set contains only one- and two-fiber populations, constructed from two prolate tensors with fixed FA value of 0.8. The ratio of voxels containing one-fiber versus two-fiber populations was set to 1:9, given that approximately 90% of the WM voxels contain “complex fiber configurations” for common voxel sizes (Jeurissen et al., 2013). VF and inter-fiber angle were the same for all the two-fiber voxels. Rician distributed noise was added to result in  $SNR = 22$  for the  $b = 0 \text{ s}/\text{mm}^2$  signal, corresponding to the SNR of the in-vivo data (see the *In vivo human brain data* section). This simulation set was used to investigate the convergence of our recursive RF calibration method. We created multiple data sets where we either varied VF or inter-fiber angle for all two-fiber populations. Ideally, the RF should converge to the DW profile of the predefined one-fiber population that was characterized by  $FA = 0.8$ . In other words, we expect that the final “FA of the RF”, estimated by fitting the diffusion tensor to the resulting RF, will approximate the FA value of the simulated single-fiber population.

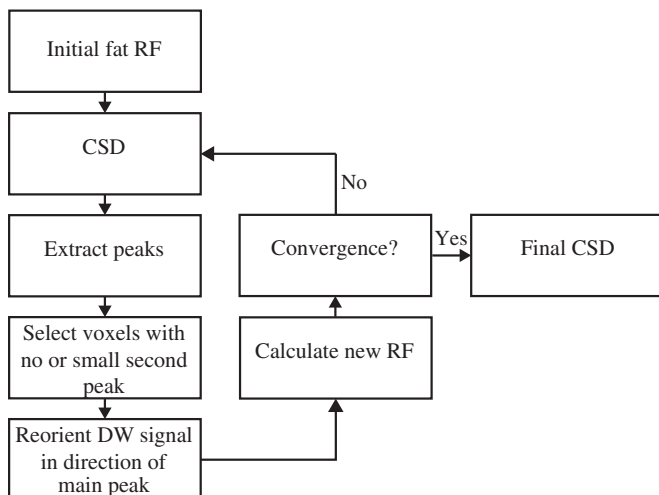


Fig. 2. Schematic overview of the recursive framework for RF estimation.

### Simulation data set (iii)

To construct the DW signals for the third simulation data set, we incorporate realistic distributions of FA values for a single fiber population, VFs, and inter-fiber angles derived from in vivo human brain data as described in [Jeurissen et al. \(2013\)](#). Specifically, one-, two- and three-fiber populations were constructed with the ratio 10:45:45. The VFs of the two-fiber populations, i.e.,  $VF_1$  and  $VF_2$ , were characterized by a Normal distribution (denoted as  $N(\mu, \sigma)$  with  $\mu$  the mean and  $\sigma$  the standard deviation), with  $VF_1$  sampled from  $N(0.5, 0.15)$  and with  $VF_2 = 1 - VF_1$ . The VFs of the three-fiber populations are sampled from the standard uniform distribution (range between 0 and 1) and subsequently normalized. Inter-fiber angles were sampled from  $N(90, 30)$  (in degrees). The FA values for the single fiber populations were sampled from either  $N(0.6, 0.05)$  – then referred to as the “FA<sub>s</sub> = 0.6” simulation data set – or  $N(0.8, 0.05)$  – then called the “FA<sub>s</sub> = 0.8” simulation data set. The purpose of this simulation data set is to investigate differences in consistency of the resulting fODF peaks with the true simulated peaks, when performing CSD with the RF calibrated either from the recursive or the FA method. An fODF peak is termed “true positive” when it has an angle difference smaller than  $5^\circ$  with a true simulated fiber. We applied an fODF threshold of 0.1 normalized to the magnitude of the first peak, and set the algorithm to detect up to 4 fODF peaks. False positives fODF peaks were all remaining peaks that did not correspond to a true simulated peak. False negative peaks were, in turn, defined as all remaining true simulated fiber populations.

### Real data

The majority of our experiments on real data were performed on an in vivo human brain data set with  $b = 2500$  s/mm<sup>2</sup> typically used for CSD ( $L_{\max} = 8$ ). In this data set we compared the recursive method with the FA method and extended findings from simulations to real data to provide guidelines for practical use. To demonstrate the general applicability of our framework, we also applied it to ex vivo data sets with different acquisition settings.

### In vivo human brain data

**Data acquisition.** A healthy volunteer (male, 25 y) was scanned on a 3.0T Philips Achieva MR scanner (Philips, Best, NL) equipped with an 8-channel receiver head coil. The subject gave informed consent to participate in this study under a protocol approved by the University Medical Center Utrecht ethics board.

First, DW images were acquired using a single-shot spin-echo echo planar imaging sequence with the following settings: acquisition matrix of  $112 \times 112$ , FOV of  $224 \times 224$  mm<sup>2</sup>, and 70 slices with a thickness of 2 mm resulting in isotropic voxels of  $2 \times 2 \times 2$  mm<sup>3</sup>. Other parameters were SENSE acceleration factor of 2 and TE/TR = 73/6718 ms. Diffusion sensitizing gradients were applied in 60 directions uniformly distributed over the hemisphere ([Jones et al., 1999](#)) with a b-value of 2500 s/mm<sup>2</sup> (NSA = 1) along with one  $b = 0$  s/mm<sup>2</sup> (NSA = 6) image. Total scan time was approximately 12 min. The SNR of the data set is 22, as estimated in WM regions of the  $b = 0$  image ([Sijbers and den Dekker, 2004](#)).

Next, a  $T_1$  image was acquired to obtain a WM mask, used in step 2) of our framework to shorten computation time. A sagittal 3D turbo field echo sequence was used with an FOV (AP  $\times$  LR  $\times$  IS) of  $240 \times 160 \times 240$  mm<sup>3</sup> and imaging matrix  $240 \times 160 \times 240$ , reconstructed to  $256 \times 160 \times 256$  matrix size with  $0.94 \times 1 \times 0.94$  mm<sup>3</sup> voxel size. A SENSE acceleration factor of 1.6 was used in both the AP and IS directions. A flip angle of  $8^\circ$  was used with TE/TR/TI = 3.5/7.6/991 ms, for a total acquisition time of 200 s.

**Image processing.** The DW scans were corrected for subject motion and eddy current induced geometric distortions including the

required B-matrix adjustments ([Leemans and Jones, 2009](#)). Processing and visualization was performed with ExploreDTI ([Leemans et al., 2009](#)).

WM voxels from the DW images were extracted using a  $T_1$  based WM mask as described previously ([Jeurissen et al., 2013](#)). In summary, a tissue probability map was estimated from the  $T_1$  image using the unified segmentation tool from SPM ([Ashburner and Friston, 2005](#)). Next, the  $T_1$  image was registered to the FA image using 3D nonrigid b-spline-based registration using Mattes mutual information ([Klein et al., 2010](#)). WM voxels in the DW image were then identified by warping the tissue probability map to the DW volume, and select voxels with WM probability higher than 95%. Finally, voxels with  $MD > \text{median}(MD) + 1.5 \cdot \text{IQR}(MD)$  were removed to avoid remaining partial voluming with CSF (where IQR is the interquartile range over the mask).

**Fiber tractography.** We performed fODF streamline tractography ([Jeurissen et al., 2011](#)) to evaluate the influence of RF calibration with both methods on tract propagation. We set an fODF and angle threshold of 0.1 and  $35^\circ$ , respectively, and a step size of 1 mm. The corpus callosum (CC, commissural fibers) was reconstructed, using the guidelines in [Wakana et al. \(2007\)](#) for defining the regions of interest.

### Ex vivo data

One human brain and one monkey spinal cord data set were used for analysis. The human brain data set was acquired in collaboration with K. Miller and consisted of 53 DWI images (NSA = 3) with  $b = 4500$  s/mm<sup>2</sup>, along with one  $b = 0$  image with  $1.2 \times 1.2 \times 1.2$  mm<sup>3</sup> voxel size. TE/TR = 20/35 ms with a flip angle of  $35^\circ$  was used. The monkey spinal cord data set consisted of 105 DWI images ( $b = 4525$  s/mm<sup>2</sup>) and 25 non-DWI images, with axial in-plane resolution of  $188 \times 188$   $\mu\text{m}^2$ , and a slice thickness of 375  $\mu\text{m}$  ([Lundell et al., 2011](#)). For more detailed acquisition parameters and image processing steps of the spinal cord and human brain data sets, the reader is referred to [Lundell et al., 2011](#) and [Miller et al., 2011](#), respectively.

The RF was calibrated with the recursive method and subsequently used to perform CSD. Appropriate selection of FA thresholds is unintuitive for these ex vivo data sets due to the intrinsically lower FA values. As such, we compared the recursive method to the FA method using two conventional approaches: 1) Define the FA threshold based on the method from [Tournier et al. \(2004\)](#), in which the voxels with the 300 highest values of FA are selected to calculate the RF; 2) Set the FA threshold as the average of FA values in a region known to have single fiber populations. For the latter approach, we have drawn ROIs in the corpus callosum of the ex vivo human brain data set, and in the WM located superior in the spinal cord of the ex vivo monkey data set.

For the monkey spinal cord data we used  $L_{\max} = 8$ ; for the human brain data  $L_{\max} = 6$  was used. In theory, 53 DW images would allow us to fit SH coefficients up to degree 8. However, as the gradient orientations were not evenly distributed on the sphere, we could only capture the angular frequencies up to degree 6 in the human brain data set.

On the human brain data set, we performed streamline tractography with fODF threshold 0.01 and step size to 0.5 mm (which differ from the in vivo human brain data set due to the higher spatial resolution and generally smaller fODF peaks). Fiber tracts of the CC, corticospinal tract (CST), and superior longitudinal fasciculus (SLF) were reconstructed at the area where they are expected to intersect each other. For the monkey spinal cord data, we were specifically interested in detecting multiple fiber populations which can be used to study commissural fibers and complex features of the gray matter and white matter collaterals ([Lundell et al., 2011](#)).

## Results

### Simulations

In this section, the results of the experiments on simulation data sets (i), (ii), and (iii) are presented in the next three sections, respectively.

#### Spurious peaks in single fiber populations

To illustrate the problem of spurious peaks, Fig. 3(a) shows the resulting fODF when a simulated single fiber population signal was deconvolved with the wrong (sharper) RF, in the case of infinite SNR (Parker et al., 2013). These spurious peaks result in erroneous tractography results, if they become too large. The median ratio of the second (spurious) peak with respect to the first peak and its upper and lower quartile ranges are shown in Fig. 3(c) in the “ideal” case, i.e., when we would have chosen exactly the right RF for deconvolution of the simulated signal. This corresponds to the diagonals of the color graphs in Fig. 3(b), which display the median ratio by a color (blue indicating a ratio of 0 and red representing a ratio of 1) for different combinations of simulated signal FA and RF-FA ranging from 0.1 to 0.9, and for different SNR values. This can be used to make an informed decision regarding the PR threshold, where the “ideal” case in Fig. 3(c) can be used as a lower bound to avoid incorrect exclusion of one-fiber populations due to spurious peaks. In the case of SNR = 22, for example, a PR threshold of 0.05 would be a reasonable choice, since 75% of the spurious peaks have a relative magnitude below this threshold for FA values greater than 0.3 and, therefore, can be considered “sufficiently small”. One can be even stricter in this threshold setting, as the RF calibration is initiated with a fat RF. Consequently, the magnitude of such spurious peaks will be even smaller.

#### Convergence of the recursive method

Fig. 4 shows the FA of the RF as function of iteration for different VF values (a) and angles (b) of the included two-fiber populations, setting a PR threshold of 0.01. For all VFs (at angle 90°), the recursive method correctly includes single fiber voxels for RF calibration, as the FA of the RF converges to 0.8 after approximately 2–4 iterations (Fig. 4(a)). Fig. 4(b) illustrates that the RF converges to the correct one for inter-

fiber angles 60° and 90° in 2–9 iterations. For inter-fiber angles of 45° and smaller, one can see that the RF converges to FA values lower than 0.8 (i.e., the calibrated RF is fatter than the true RF). This means that in the two-fiber voxels, with angles of 45° and smaller between the two fiber orientations, only one peak could be detected. Consequently, these voxels were not correctly excluded from the RF calibration.

#### Comparison of angular consistency between recursive and FA method

Figs. 5(a, c) and (b, d) display the results for the simulation sets with FA<sub>s</sub> = 0.8 and FA<sub>s</sub> = 0.6, respectively. In Figs. 5(a) and (b), we plotted the sensitivity (ratio of true positive fODF peaks to the sum of true positive and false negative peaks) against the number of false positives as a function of the threshold value (circled points). The colored lines represent different SNR values. The top plots in Figs. 5(a) and (b) show results for the FA method with FA threshold ranging from 0.1 to 0.9 in steps of 0.1 (in Fig. 5(b) FA ranged from 0.1 to 0.8, since there were no voxels with FA higher than 0.9 for the different SNR levels). The bottom plots show the results for the recursive method (with PR threshold values = [0.5, 0.2, 0.1, 0.05, 0.02, 0.01, 0.005]).

In Fig. 5(a), one can see that for high SNR (15 to 30), the change in sensitivity and number of false positives for the recursive method is almost independent of the PR threshold, despite a 100-fold increase (from 0.005 to 0.5). For the FA method, on the other hand, this is not the case. One can notice that for the FA method at high SNR, the amount of false positives is high at a low FA threshold, drops down, and subsequently increases again with increasing FA threshold. When using a fatter RF (and thus low FA threshold), angular deviation of fODF peaks with true peaks will be larger, which results in more false positives. An RF that is too sharp will result in spurious peaks, which will be counted as false positives. The graphs of the FA method and recursive method overlap for the same SNR, which implies that the same sensitivity and specificity can be reached with both methods. The recursive method, however, yields optimal sensitivity and specificity values that are less dependent on the PR threshold at high SNR.

In Fig. 5(b), there is an overall decrease of sensitivity and increase of false positives for the data set with lower FA (FA<sub>s</sub> = 0.6) for a single fiber population. One can again notice the higher robustness of the

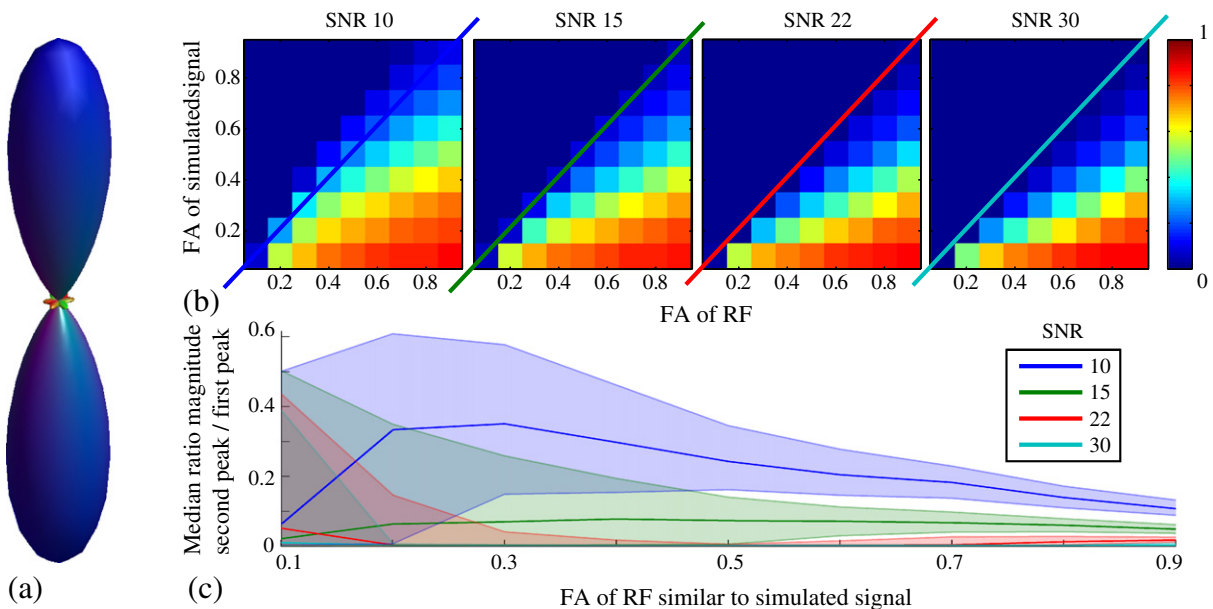


**Fig. 3.** Results of simulation set (i). (a) Illustration of spurious peaks occurring when the RF is not properly chosen. Here, the resulting fODF is shown for a simulated signal with FA = 0.5 (infinite SNR) and an RF with FA = 0.8. (b) CSD of a single fiber population simulated as a tensor with a particular FA (vertical axis) with an RF (also a tensor with chosen FA, horizontal axis) gives spurious peaks. Here the median relative magnitude of the second (spurious) peak compared to the first (true) peak is shown in color for all combinations of simulated signal- and RF-FA (Parker et al., 2013), for SNR = [10, 15, 22, 30]. (c) For the ideal case, where the RF has exactly the same shape as the simulated signal (same FA), the median relative magnitude of the spurious peak is visualized together with  $Q_1$  and  $Q_3$  for different FAs. This corresponds to the diagonals of (b).

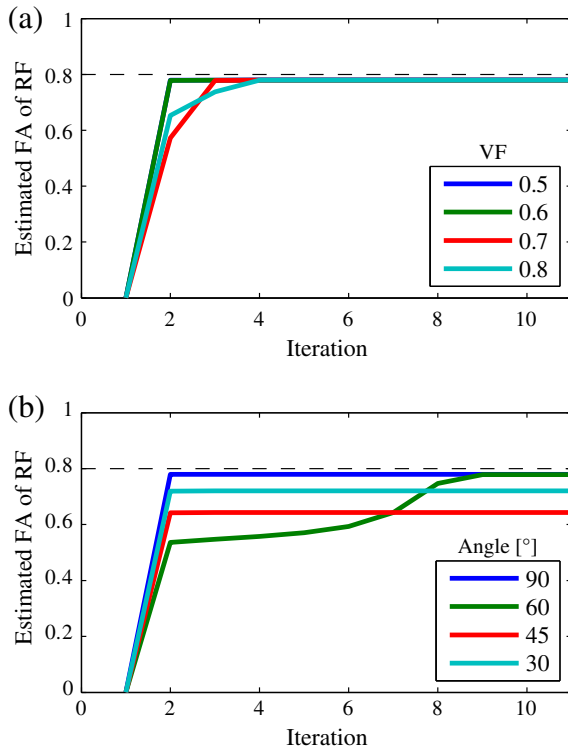


**Fig. 4.** Results of simulation set (ii). FA of the RF over iteration for (a) different volume fractions with a 90° angle, and (b) different angles with equal volume fractions for the included two-fiber voxels. Dashed line represents the FA of a simulated single fiber population. We set PR threshold = 0.01. For the data sets that include two-fiber populations crossing at 45° or 30° in (b), one can see that the two-fiber voxels cannot be distinguished from one-fiber voxels and, therefore, will also be selected for RF estimation, which results in a fatter RF and thus lower FA of the RF.

recursive method towards the PR threshold. The main result here is that the PR thresholds that yield the highest sensitivity and specificity in the recursive method are independent of the simulated fiber FA of the underlying data set, when comparing Figs. 5(a) to (b). For instance, a peak threshold of 0.01 or 0.005 for SNR 22 would give a good trade-off between sensitivity and number of false positives in both the FA<sub>s</sub> = 0.8 and the FA<sub>s</sub> = 0.6 data sets, whereas one should use different FA thresholds (0.7 and 0.5, respectively) to obtain the same sensitivity and number of false positives with the FA method.

Figs. 5(c) and (d) show histograms of the angle between the main fODF peak and its closest true simulated peak at an SNR of 22 for the FA<sub>s</sub> = 0.8 and the FA<sub>s</sub> = 0.6 data sets, respectively (top rows: FA method; bottom rows: recursive method). It can be observed that for the FA method, an FA threshold of 0.8 and 0.6 would result in the smallest median angle deviation for the FA<sub>s</sub> = 0.8 and FA<sub>s</sub> = 0.6 data sets, respectively. By contrast, a peak threshold of 0.005 yields the smallest median angle deviation for both simulation data sets (FA<sub>s</sub> = 0.8 and FA<sub>s</sub> = 0.6) using the recursive method.

## Real data

### In vivo human brain data

In Fig. 6(a), the method is illustrated on the in vivo human data for a PR threshold of 0.01. The graph represents the number of voxels included for RF calibration as a function of iteration, convergence is reached after ten iterations. The resulting fODFs in the centrum semiovale are visualized for iteration one, two, and ten. We start off with a fat RF and all WM voxels derived from the T<sub>1</sub>. The resulting fODFs show secondary peaks in voxels with crossing fiber populations of approximately equal volume fractions. These voxels will be discarded from the RF calculation

in the first iteration. For the second iteration, we end up with an RF that is flatter, and deconvolution yields secondary and tertiary peaks in voxels with multiple fiber populations of unequal VF. fODF peaks of single fiber populations become larger. After ten iterations, the algorithm has converged and the number of voxels used for RF calculation remains unchanged. Fig. 6(b) top shows which voxels are selected in each iteration (up to 10 iterations). The brightest voxels are used for final RF calculation, and comprise a range of FA values (0.3–1) with a mean of 0.67, as can be seen from the histogram in Fig. 6(b) bottom. Lower FA voxels are thus also selected, while some high FA voxels are discarded as can be seen by comparing the map of Fig. 6(b) top to the FA map in (c).

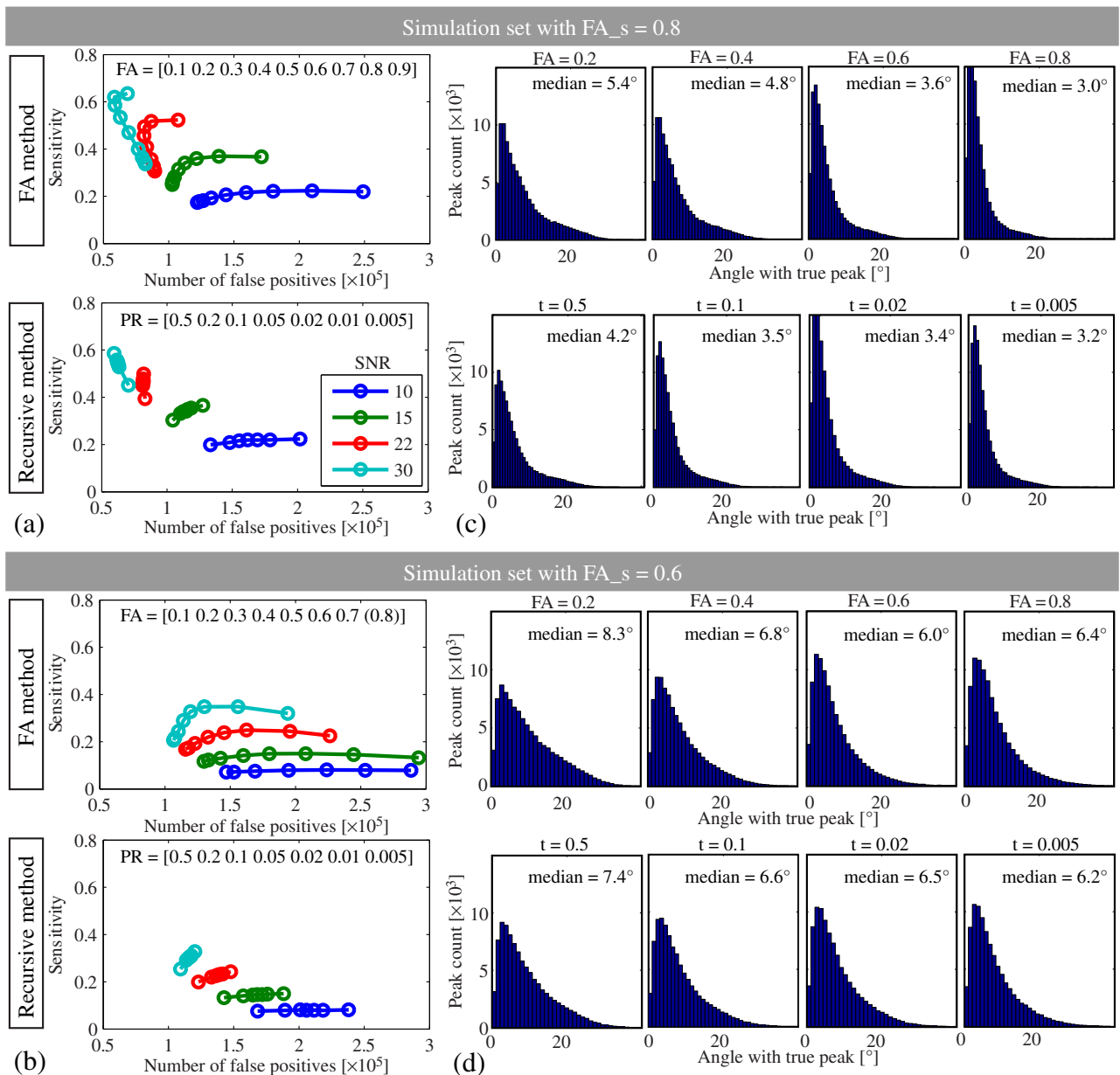
The recursive method and FA method are compared in Fig. 7. The figure shows the angle differences between the main peak orientations, both in histograms (whole brain) and in color plots (ROI as indicated in Fig. 7(a)). Fig. 7(b) shows the angle difference when comparing two different thresholds (0.01 and 0.05) within the recursive method. Fig. 7(c) shows the same figure for two different thresholds (0.7 and 0.8) within the FA method. Note that a five-fold increase of the peak threshold (from 0.01 to 0.05) yields a smaller median angle difference (median = 0.5°) than the median angle difference when comparing FA threshold 0.7 to 0.8 using the FA method (median = 0.7°, see Fig. 7(c)). This supports simulation results indicating increased robustness of the recursive method towards its PR threshold value. Figs. 7(d–g) compare different thresholds between methods. One can see that between the recursive and FA method, fODF peaks obtained with PR threshold = 0.01 and FA threshold = 0.7 are the most comparable for this particular data set (median = 0.5° in Fig. 7(d)).

Fig. 8 shows the results of fODF streamline tractography of the CC, for both the FA method (FA threshold = [0.7, 0.8]) and the recursive method (PR threshold = [0.01, 0.05]). The difference between both methods can be appreciated in the region of the centrum semiovale, where the lateral projections of the CC are delineated more completely using the recursive method.

### Ex vivo data

Fig. 9 shows the results for the ex vivo human brain data set. In Fig. 9(a), the fODFs reconstructed with the recursive method are shown in a region as indicated in Fig. 9(b). Figs. 9(c) and (e) show the same region for the FA method, using the two different approaches for selecting the FA threshold: 1) the 300 highest FA voxels and 2) the average FA value in a region of the CC. The FA thresholds for approaches 1) and 2) were 0.67 and 0.48, respectively. Although differences in the fODFs are very subtle between (a) and (c), the fODFs clearly differ in magnitude and direction compared to (e). Differences become more prominent for the tractography results. We were able to track the CST, CC and SLF (see Fig. 9(b) for the recursive method, and (d) and (f) for the FA method, showing a coronal view left and a sagittal view right), despite the major challenges in these crossing fiber regions that are known to exist for ex vivo data (Miller et al., 2011). Using the recursive method, the lateral projections of the CC could be reconstructed with greater detail when comparing Fig. 9(b) left with Figs. 9(d) and (f) left (white arrows). Although the SLF pathways extend more anteriorly using the FA method, there are trajectories that deflect into other regions (see white arrows in right image in (d) and (f)) or there seem to be parts that are missing (see yellow arrow in right image in (d) and (f)).

In Fig. 10, results for the ex vivo monkey spinal cord are displayed. For visualization purposes, we performed DTI streamline tractography (Basser et al., 2000; Lundell et al., 2011) as shown in Fig. 10(a) in a dorsal coronal view, with most fibers oriented inferiorly–superiorly. Figs. 10(b) and (c) show two transversal slices of interest for both the recursive and the FA method, one at the location of the cervical enlargement (bottom three) and one more superiorly (top three). For each slice, the recursive method is compared to the FA method where the FA threshold was determined using the two different approaches. The FA thresholds for approaches 1) and 2) were 0.82 and 0.59, respectively.



**Fig. 5.** Results of simulation set (iii). We used mean  $FA_s = 0.8$  for the distribution of a single fiber population for (a) and (c), and  $FA_s = 0.6$  for (b) and (d), respectively. (a) Top: Sensitivity of the FA threshold method against the number of false positives for FA threshold [0.1–0.9] in steps of 0.1, for different SNR values. The point with the lowest sensitivity corresponds to  $FA = 0.1$ . Bottom: Same graph for the recursive method with PR threshold values = [0.5, 0.2, 0.1, 0.05, 0.02, 0.01, 0.005], the point with the lowest sensitivity corresponds to PR threshold = 0.5. (b) The recursive and FA methods for RF calibration are used on the data set with mean  $FA_s = 0.6$  for a single fiber population. For SNR 10, there were no voxels with  $FA > 0.8$ . (c) and (d) Histograms of the angle between the main fODF peak and its closest true simulated peak at SNR 22 for data sets  $FA_s = 0.8$  and  $FA_s = 0.6$ , respectively, and for the FA (top row) and recursive (bottom row) methods, separately.

Fig. 10(b) shows the inferiorly–superiorly oriented largest fODF peaks, whereas Fig. 10(c) shows both the second and third fODF peaks. The radial organization in the WM and commissural connections in the gray matter can be appreciated in both slices for both the recursive and the FA method. In analogy to Lundell et al. (2011), we found that more crossing fibers could be found when moving closer to the cervical enlargement. Note the difference in crossing fibers for the FA method between the two different thresholds. It can also be seen in both slices that the FA method with threshold 0.82 reveals more crossing fibers than both the FA method with the lower threshold and the recursive method.

## Discussion

Spherical deconvolution based techniques are appealing to tackle the crossing fiber problem, as they provide a balanced trade-off between

constraints on the required hardware performance and acquisition time on the one hand, and the reliability of the reconstructed fODF on the other hand. The underlying assumption for most SD techniques is that there is a single appropriate RF throughout the whole brain, which is not known a priori. Although it is questionable whether there actually exists one RF for the whole brain (and not a distribution of one-fiber RFs instead), it provides computational advantages to assume so.

Recent work has extensively investigated the effect of RF miscalibration on the resulting fODFs (Parker et al., 2013). Besides angular deviations, an overestimation in RF anisotropy will lead to predictable spurious fODF peaks in true single fiber populations due to truncation of the SH series. Their work states that a more informed calibration might lead to vast improvements in results, for example in cases of WM degradation and other fibrous tissue, where it is difficult to make an assumption about the RF a priori.

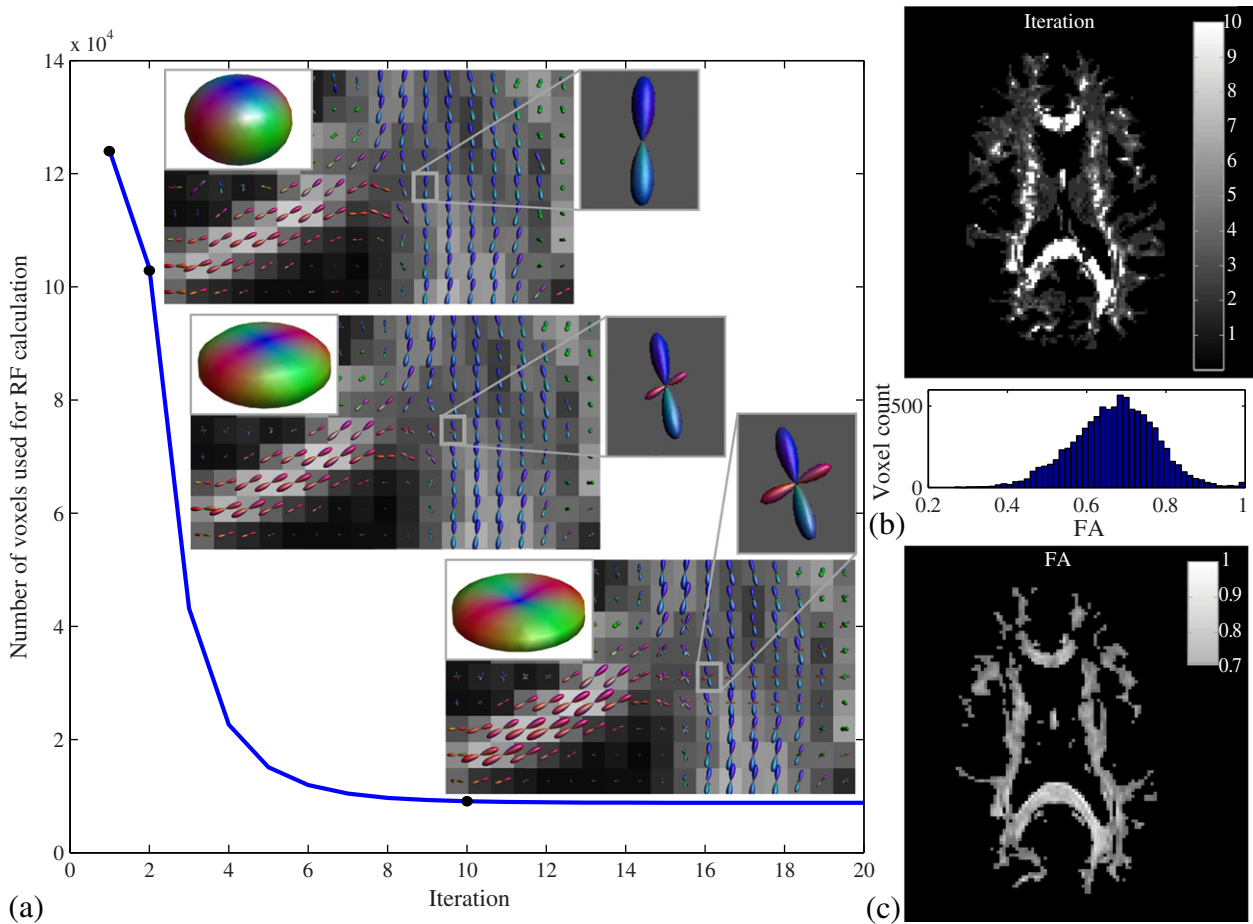


**Fig. 6.** Illustration of the method on real human data, using PR threshold = 0.01. (a) Number of voxels used for RF calibration, together with the used RF and the resulting fODFs, as function of iteration. (b) Top: Voxels selected in different iterations, visualized up to iteration 10. The brightest voxels are used for final RF calculation. Bottom: Histogram of the FA of the voxels used for final RF calculation. (c) FA > 0.7 map.

The RF could be modeled by axial symmetric tensors on a voxel-by-voxel basis (Anderson, 2005), but it is well known that the DW signal deviates significantly from this model at high b-values, even in single fiber populations. The FA method therefore determines the RF from the signal itself, by averaging the signal in high FA voxels. We will discuss the drawbacks of this method in the following paragraphs, which the recursive method tries to address.

#### Dependence on the diffusion tensor model

Although CSD itself is not based on the tensor model, the conventional calibration step (the FA method) still is. It uses the FA to select voxels for RF calibration, and the first eigenvector of the diffusion tensor to rotate the DW signal before averaging. Besides the violation of the assumption of Gaussianity at high b-values, the accuracy of FA and eigenvector estimates in this low SNR regime is poor. The choice of diffusion tensor estimation procedure (e.g., ordinary-, weighted-, and non-linear-least squares) may play a role, especially if gross artifacts are present (as data outliers may produce artificially high FA values), which will contaminate the RF estimation. Noteworthy is that the recursive framework presented in this work is completely independent of DTI based measures.

#### Dependence on underlying data properties

For the FA method, it is difficult to make an assumption about which FA to choose for RF calibration, especially in the case of white matter degradation, neuro-development, or when other types of fiber tissue

are investigated. Due to the unknown anisotropy of underlying tissue, the results with the FA method are very dependent on the predefined FA threshold setting. In our framework, we can make a more informed decision by setting the PR threshold, and the method furthermore shows to be robust towards this threshold.

By setting the PR threshold, we impose the relative magnitude of the secondary fODF peak compared to the first fODF peak that would still be allowed for a voxel being classified as one-fiber voxel. For true single fiber populations, we approximately know what spurious peak-magnitudes to expect at a given SNR (see Fig. 3), and adapt the PR threshold accordingly. A lower bound PR threshold may be set at which spurious peaks in one fiber populations can still be distinguished from true multiple-fiber voxels. For reasonable SNR levels (15 to 30), this minimal threshold is almost independent of the FA of underlying tissue (Figs. 3 and 5). For SNR 22, for example, a PR threshold of 0.05 would correctly select one-fiber voxels for RF estimation in the case of a “perfectly” chosen RF. In practice, however, we start off with a fat RF and spurious peaks will be smaller, so one could even be very strict in this threshold setting (for example, setting it to 0.01 or 0.005, see Fig. 5).

We have shown that our recursive framework for RF estimation is more robust than the FA method towards differences in anisotropy of underlying tissues for high SNR (see Fig. 5). For both the  $FA_s = 0.6$  and  $FA_s = 0.8$  simulation data sets, the same PR threshold of 0.005 yields the minimal difference in angle between the main fODF peaks and the true simulated peaks. This is supported by our evaluations on real data. The ex vivo human brain data has intrinsically lower FA values than the in vivo data (0.32 in the CC according to previous work by Miller et al., 2011), and the ex vivo spinal cord data has a mean FA of

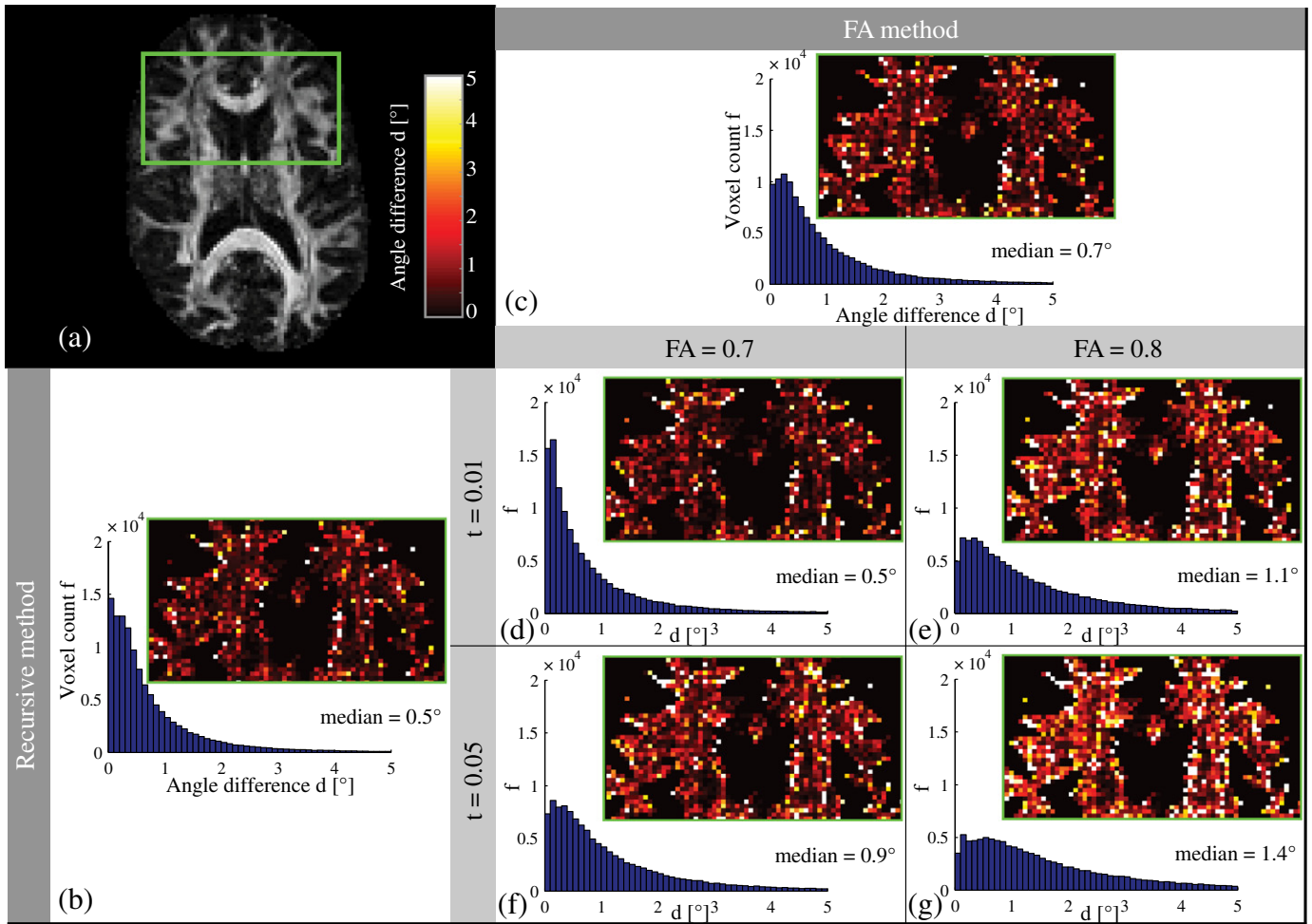


**Fig. 7.** Histograms of the angle difference  $d$  between the main peak orientations. ROIs in (b–g) are chosen as indicated in (a). (b) Comparison of main peak orientations for different thresholds using the recursive method. (c) Same as (b) for the FA method. (d–g) Comparison of both methods, different thresholds.

approximately 0.53 in the WM as estimated by Lundell et al. (2011). Despite the difference in underlying diffusion properties between these data sets, we were able to generate plausible results with the recursive RF calibration using the same PR threshold of 0.01. As demonstrated in Figs. 9 and 10, such uniformity could not be realized by a single threshold setting for the FA. The results for the FA method show that selecting an FA threshold with two plausible approaches already gives very different results. Selecting the 300 highest FA voxels is still quite ad-hoc (why 300, and

how will this choice affect the results?) and selecting an ROI to determine the FA threshold can be very rater-dependent.

In the ex vivo human brain data, tractography on the fODFs obtained with the FA method resulted in missing and deflecting tracts. If the FA threshold is taken too low, the fODFs are smaller in magnitude, the number of false negative peaks is larger, and the fODFs have a lower angular resolution. In the ex vivo monkey spinal cord data, a radial organization of the WM and commissural connections in the gray matter were

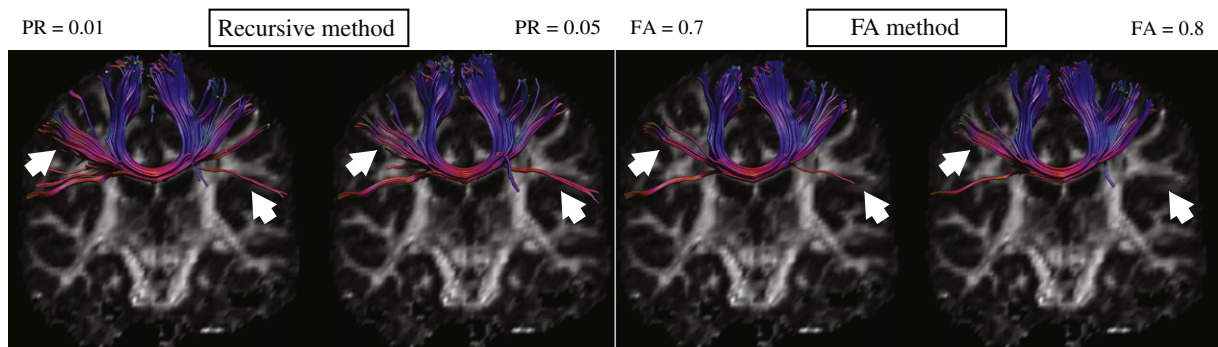


**Fig. 8.** Tractography results of CC using RF estimation with both methods, for different PR and FA thresholds, respectively. The recursive method reveals the lateral projections of the corpus callosum better (arrows).

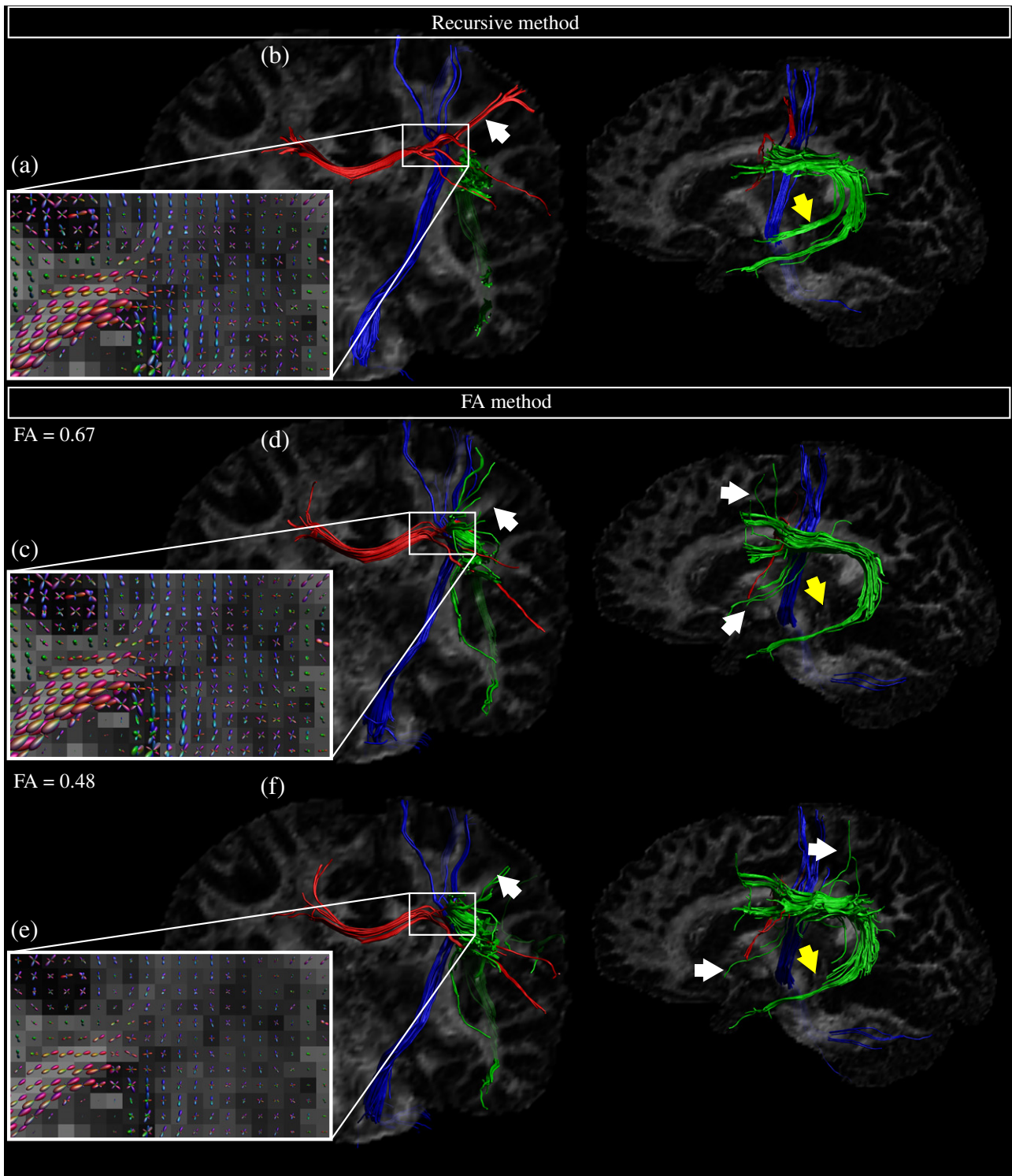


**Fig. 9.** Results of CSD with the RF resulting from the recursive method (PR threshold = 0.01) compared to the FA method (two different threshold approaches) for the ex vivo human brain data. (a, c, e) fODFs visualized in the centrum semiovale, where the CC, CST and SLF pathways intersect each other. fODFs in (a) and (c) look similar, but in (e) they differ a lot in direction and magnitude. (b, d, f) Streamline tractography of the CC (red), CST (blue) and SLF (green), in a coronal (left) and sagittal (right) view. White arrows in the coronal view indicate difference in lateral projections of the CC. In the sagittal image, white arrows show false positive pathways of the SLF, whereas yellow arrows indicate missing areas.

found with both RF calibration methods. The highest number of fODF peaks could be found using the FA method with the highest FA threshold. Note, however, that one always needs to make a trade-off between sensitivity and specificity, which relies heavily on the choice of FA threshold. Though the sensitivity with this FA threshold appears to be higher compared to the recursive method in this case, the number of false positives (spurious or deflecting peaks) increases with a higher

FA threshold. We thus argue that when no reliable assumption can be done on the underlying FA of the tissue, the recursive method should be the method of choice.

For the FA method, sensitivity and number of false positive fODF peaks change significantly between different FA thresholds, even at the high SNR of 30 (see Fig. 5) and despite the relatively small change in FA threshold. When comparing this to the recursive method,

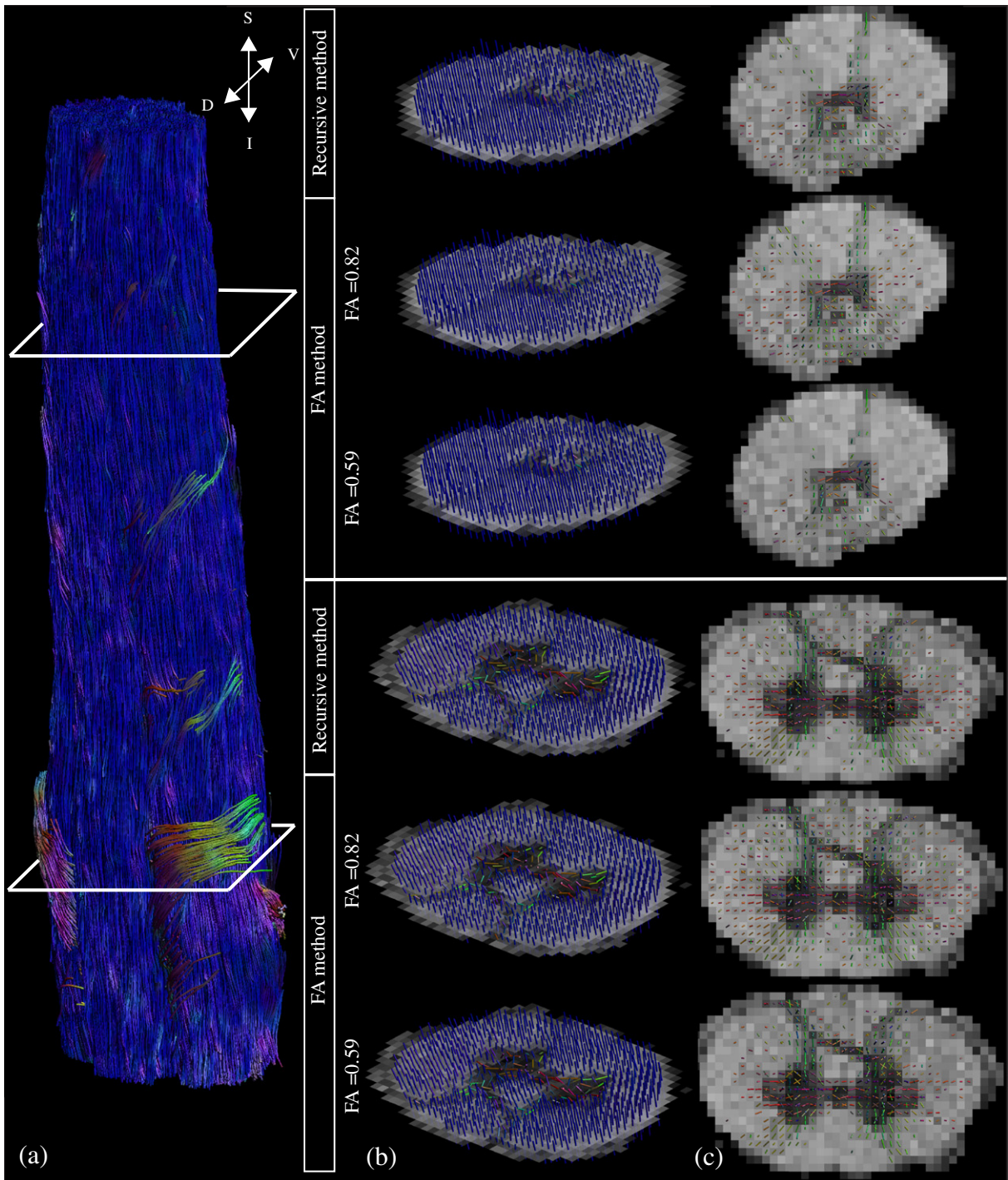


**Fig. 10.** (a) Tractography of the ex vivo monkey spinal cord to highlight the location of the two transversal slices shown in (b) and (c). Results of CSD are visualized by means of the first peak (b) and the second and third peaks (c). Results are shown for both the recursive (PR threshold = 0.01) and FA method (with two different FA threshold approaches). In the middle row of each slice, the FA threshold was determined by the 300 highest FA voxels, whereas in the bottom row, the FA threshold was based on the ROI.

sensitivity and number of false positives do not change a lot for a relatively large change in PR threshold. More specifically, at  $\text{SNR} = 22$ , sensitivity and number of false positives increase by 0.01 and 637, respectively, when decreasing the PR threshold from 0.05 to 0.01, which is a five-fold decrease. This observation is also supported by experiments on human data, where the angle difference between the main fODF peaks is smaller for the recursive method when changing the PR threshold from 0.05 to 0.01 than for the FA method when changing the FA threshold from 0.7 to 0.8. For low SNR data, which is known to be difficult for SD methods (Fillard et al., 2011; Tournier et al., 2013),

one should make an informed decision balancing between decreased specificity and increased number of false positives.

#### Convergence

Since the RF calibration in our proposed method is recursive, it is important to investigate its convergence properties. As shown by the simulation experiment in Fig. 4, the algorithm converges towards the predefined profile of a single fiber population after roughly nine iterations. For all VFs with fiber orientations crossing at an angle of  $90^\circ$ , the

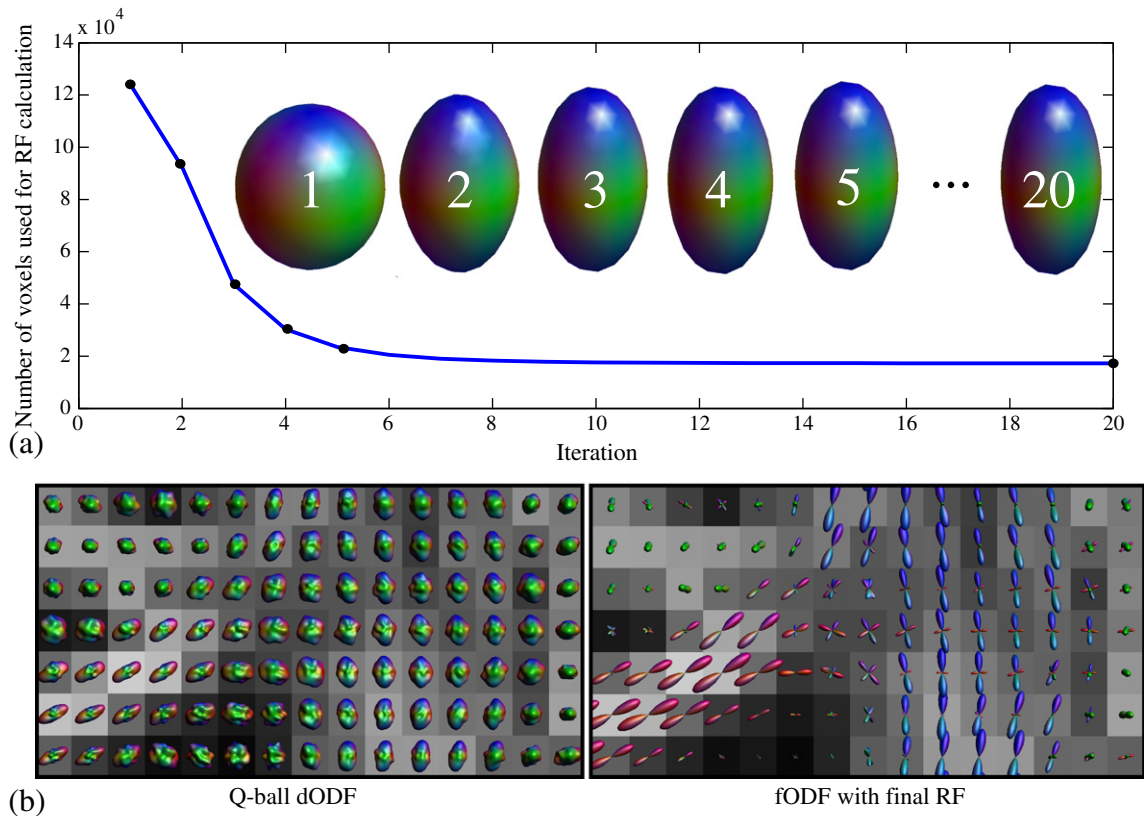


**Fig. 11.** Q-ball dODF sharpening, where the RF is calibrated with our recursive approach. (a) Number of voxels used for RF calibration as a function of iteration number, showing convergence after roughly 8 iterations. The RF represents in this case the dODF of a one-fiber profile and is shown as function of iteration. (b) Left: Q-ball dODFs; right: sharpened fODFs after SDT.

FA of the RF converges to 0.8 (see Fig. 4(a)). For equal VFs and inter-fiber angles of  $60^\circ$  and  $90^\circ$ , the RF converges also correctly, but for inter-fiber angles of  $45^\circ$  and smaller, one can see that the two-fiber voxels were not correctly excluded from RF calibration, resulting in an FA value of the RF lower than 0.8 (i.e., a fatter RF than the true one – see Fig. 4(b)).

The recursive method assumes that fODFs with a single significant peak are unambiguously associated with a single fiber orientation. However, it is well-known that for some configurations, like fanning and bending fibers as well as crossing fibers with low VF or small separation angle, only a single FOD peak can be detected, irrespective of the underlying true response function profile. As a result, inclusion of voxels with such configurations will affect the RF calibration in the sense that it will become fatter than the true RF, ultimately leading to a lower angular resolution (Parker et al., 2013). This effect becomes more apparent when relatively few “true single fiber populations” are present in the data. Furthermore, Tournier et al. (2007) state that, under specific simulation conditions (b-value of  $3000 \text{ s/mm}^2$ , SNR 20, 60 directions and exact RF), CSD cannot resolve fiber populations separated by angles smaller than  $40^\circ$  in a reliable way. Regarding the simulations in Fig. 4(b), given our simulation settings (with a lower b-value of  $2500 \text{ s/mm}^2$ , non-exact RF, and inclusion of 90% two-fiber voxels as described in Simulation data set (ii)), it is to be expected that angles below  $45^\circ$  cannot be distinguished correctly from a single fiber population.

For the analyses on the in/ex vivo human brain data and the ex vivo spinal cord data, the recursive method converged after eight to ten iterations. For the human brain data, processing time for the RF calibration is in the order of five min.

#### Voxels used for RF calibration

For in vivo human data, the voxels that are eventually selected for RF calculation comprise FA values ranging from roughly 0.3 to 0.9 (see Fig. 6); hence, the final RF is not simply the average of high FA voxels.

The FA values are approximately normally distributed with mean 0.67 and standard deviation 0.10. This indicates that there are single fiber populations in voxels with FA values smaller than 0.7 (which was confirmed by visual inspection); voxels that would otherwise have been discarded from RF calibration. As the initial distribution of all WM voxels has mean FA  $0.37 (\pm 0.17)$  and is slightly positively skewed, a large amount of low FA voxels are discarded from RF calculation. One has to keep in mind, however, that the reliability of FA estimates is low at high b-values. In the WM, 25.2% of the  $FA > 0.7$  voxels have a peak ratio larger than 0.01, which is a significant amount and thus lends further support to the proposed method.

#### Potential impact for group studies

Selecting the correct RF is an important factor for SD approaches (Parker et al., 2013). Typically, most SD methods perform the RF calibration in a data driven way and for each data set separately. An alternative approach is to model the RF (e.g., defined as the DW signal profile that corresponds to an axially symmetric diffusion tensor with a specific FA and MD value) and keep it constant for each data set. With the advent of SD based quantitative measures, such as “apparent fiber density” (Raffelt et al., 2012) and “hindrance modulated orientational anisotropy” (Dell’Acqua et al., in press), there are several factors related to the RF calibration step that could impact the validity of these new measures in group studies.

It is, for instance, not clear how pathology or age-related changes would affect the RF calibration and, in turn, how that would drive the final estimates of the diffusion metrics. This concern raises the question whether the RF should be computed for each data set separately, at a group level, or even across groups. And if the latter, there are many ways to achieve an “average RF”, adding more unknowns to the equation. Averaging, however, may not be optimal either, since the group RF could differ from the true RF for each subject. Alternatively,

differences in diffusion properties between groups could even be reflected in the calibrated RF itself and, hence, comparing the RF between groups may provide us with useful information. Which RF calibration approach would be optimal for group studies remains an open question and would be an interesting topic for future investigations. Note that the above concerns are not specific to our proposed recursive framework for RF calibration, but related to SD methods in general.

#### Limitations and possible improvements

Although our method has proven to overcome some of the limitations of FA method, there is room for improvement. The method still results in a single RF for the whole brain, which is likely an oversimplification. Theoretically, the recursive method could be applied on distinct brain regions to calibrate an individual RF that best “fits” that particular region. In this way, we would not stick to one RF for the whole brain, but instead tune the RF for distinct brain regions. This would, however, result in a trade-off between spatial specificity and RF stability due to the lower number of included WM voxels. More importantly, one may wonder whether the RF will vary only spatially, or whether it is more likely to vary from one to another fiber population in the same region.

Although CSD is the method of choice for SD in this work, there are also other implementations for SD approaches (Alexander, 2005; Anderson, 2005; Dell'Acqua et al., 2007, 2010; Descoteaux et al., 2009). To demonstrate that our approach is more generally applicable, we performed an extra analysis in which the sharpening deconvolution transform (SDT) method of Descoteaux et al. (2009) was used. In contrast to the CSD method, where the RF represents the diffusion-weighted signal of a single fiber orientation, the SDT approach uses the dODF of a one-fiber profile as the RF. As such, our algorithm was initialized with a dODF of a fat tensor ( $FA = 0.05$ , see Fig. 11(a)) and the PR threshold was set to 0.01. Spherical deconvolution of the Q-ball dODFs with the final calibrated RF then produces the fODFs (Fig. 11(b)). The framework can also be extended to non-SH-based methods. The (damped) Richardson-Lucy (RL) SD (Dell'Acqua et al., 2007, 2010), for instance, does not use a spherical harmonic basis. Choosing the RF for RL-based SD may serve as a trade-off between angular resolution and noise stability with sharper RF profiles providing higher angular resolutions at the cost of lower stability (Parker et al., 2013). Hence, the recursive RF calibration procedure proposed in this work could also offer a valuable fine-tuning for the RL-based SD method.

#### Conclusion

In this paper, a novel RF calibration method for SD approaches was presented. This method was compared to the commonly used method of calculating a mean RF of selected voxels with a range of FA values. Our recursive method has proven to overcome some of the limitations of the previously mentioned FA method and is completely independent of the diffusion tensor model. Voxels are selected for RF calibration when their fODFs have a sufficiently small or absent second peak as defined by the PR threshold, which allows us to make an informed and balanced trade-off between sensitivity and specificity of the fODF peaks. The method is robust and for SNR levels around 20, we recommend a PR threshold of 0.01. We have shown that CSD with the recursive RF calibration approach yields plausible results in a variety of imaging data sets, both in vivo and ex vivo.

#### Acknowledgments

We would like to thank Laurena Holleran and Karla L. Miller for providing the ex vivo human brain data, and Tim B. Dyrby for the use of the monkey spinal cord data. Furthermore, the authors thank Eleftherios Garyfallidis for the useful discussion on the sharpening deconvolution

transform method. The research of Chantal Tax is supported by an FC-EW grant (No. 612.001.104) from the Dutch scientific foundation NWO.

#### Conflict of interest

The authors have no conflict of interest to declare.

#### References

- Alexander, D.C., 2005. Maximum entropy spherical deconvolution for diffusion MRI. *Inf. Process. Med. Imaging* 19, 76–87.
- Alexander, A.L., Hasan, K.M., Lazar, M., Tsuruda, J.S., Parker, D.L., 2001. Analysis of partial volume effects in diffusion-tensor MRI. *Magn. Reson. Med.* 45, 770–780.
- Anderson, A.W., 2005. Measurement of fiber orientation distributions using high angular resolution diffusion imaging. *Magn. Reson. Med.* 54, 1194–1206.
- Ashburner, J., Friston, K.J., 2005. Unified segmentation. *Neuroimage* 26, 839–851.
- Assaf, Y., Freidlin, R.Z., Rohde, G.K., Basser, P.J., 2004. New modeling and experimental framework to characterize hindered and restricted water diffusion in brain white matter. *Magn. Reson. Med.* 52, 965–978.
- Basser, P.J., Mattiello, J., LeBihan, D., 1994. Estimation of the effective self-diffusion tensor from the NMR spin echo. *J. Magn. Reson. B* 103, 247–254.
- Basser, P.J., Pajevic, S., Pierpaoli, C., Duda, J., Aldroubi, A., 2000. In vivo fiber tractography using DT-MRI data. *Magn. Reson. Med.* 44, 625–632.
- Beaulieu, C., 2002. The basis of anisotropic water diffusion in the nervous system – a technical review. *NMR Biomed.* 15, 435–455.
- Carballedo, A., Amico, F., Ugwu, I., Fagan, A.J., Fahey, C., Morris, D., Meaney, J.F., Leemans, A., Frodl, T., 2012. Reduced fractional anisotropy in the uncinate fasciculus in patients with major depression carrying the met-allele of the Val66Met brain-derived neurotrophic factor genotype. *Am. J. Med. Genet. B Neuropsychiatr. Genet.* 159B, 537–548.
- Clark, C.A., Le, B.D., 2000. Water diffusion compartmentation and anisotropy at high b values in the human brain. *Magn. Reson. Med.* 44, 852–859.
- De Groof, G., Verhoye, M., Poirier, C., Leemans, A., Eens, M., Darras, V.M., Van der Linden, A., 2009. Structural changes between seasons in the songbird auditory forebrain. *J. Neurosci.* 29, 13557–13565.
- Dell'Acqua, F., Scifo, P., Clarke, R.A., Scotti, G., Fazio, F., 2007. A model-based deconvolution approach to solve fiber crossing in diffusion-weighted MR imaging. *IEEE Trans. Biomed. Eng.* 54, 462–472.
- Dell'Acqua, F., Scifo, P., Rizzo, G., Catani, M., Simmons, A., Scotti, G., Fazio, F., 2010. A modified damped Richardson-Lucy algorithm to reduce isotropic background effects in spherical deconvolution. *Neuroimage* 49, 1446–1458.
- Dell'Acqua, F., Simmons, A., Williams, S.C., Catani, M., 2013. Can spherical deconvolution provide more information than fiber orientations? Hindrance modulated orientational anisotropy, a true-tract specific index to characterize white matter diffusion. *Hum. Brain Mapp.* (in press).
- Descoteaux, M., Angelino, E., Fitzgibbons, S., Deriche, R., 2007. Regularized, fast, and robust analytical Q-ball imaging. *Magn. Reson. Med.* 58, 497–510.
- Descoteaux, M., Deriche, R., Knosche, T.R., Anwander, A., 2009. Deterministic and probabilistic tractography based on complex fibre orientation distributions. *IEEE Trans. Med. Imaging* 28, 269–286.
- Emsell, L., Leemans, A., Langan, C., Van, H.W., Barker, G.J., McCarthy, P., Jeurissen, B., Sijbers, J., Sunaert, S., Cannon, D.M., McDonald, C., 2013. Limbic and callosal white matter changes in euthymic bipolar I disorder: an advanced diffusion magnetic resonance imaging tractography study. *Biol. Psychiatry* 73, 194–201.
- Fillard, P., Descoteaux, M., Goh, A., Gouttard, S., Jeurissen, B., Malcolm, J., Ramirez-Manzanares, A., Reisert, M., Sakaie, K., Tensaouti, F., Yo, T., Mangin, J.F., Poupon, C., 2011. Quantitative evaluation of 10 tractography algorithms on a realistic diffusion MR phantom. *Neuroimage* 56, 220–234.
- Frank, L.R., 2002. Characterization of anisotropy in high angular resolution diffusion-weighted MRI. *Magn. Reson. Med.* 47, 1083–1099.
- Hess, C.P., Mukherjee, P., Han, E.T., Xu, D., Vigneron, D.B., 2006. Q-ball reconstruction of multimodal fiber orientations using the spherical harmonic basis. *Magn. Reson. Med.* 56, 104–117.
- Jeurissen, B., Leemans, A., Jones, D.K., Tournier, J.D., Sijbers, J., 2011. Probabilistic fiber tracking using the residual bootstrap with constrained spherical deconvolution. *Hum. Brain Mapp.* 32, 461–479.
- Jeurissen, B., Leemans, A., Tournier, J.D., Jones, D.K., Sijbers, J., 2013. Investigating the Prevalence of Complex Fiber Configurations in White Matter Tissue With Diffusion Magnetic Resonance Imaging.
- Jones, D.K., Basser, P.J., 2004. “Squashing peanuts and smashing pumpkins”: how noise distorts diffusion-weighted MR data. *Magn. Reson. Med.* 52, 979–993.
- Jones, D.K., Horsfield, M.A., Simmons, A., 1999. Optimal strategies for measuring diffusion in anisotropic systems by magnetic resonance imaging. *Magn. Reson. Med.* 42, 515–525.
- Klein, S., Staring, M., Murphy, K., Viergever, M.A., Pluim, J.P., 2010. elastix: a toolbox for intensity-based medical image registration. *IEEE Trans. Med. Imaging* 29, 196–205.
- Langen, M., Leemans, A., Johnston, P., Ecker, C., Daly, E., Murphy, C.M., Dell'Acqua, F., Durston, S., Murphy, D.G., 2012. Fronto-striatal circuitry and inhibitory control in autism: findings from diffusion tensor imaging tractography. *Cortex* 48, 183–193.
- Le Bihan, D., Breton, E., Lallemand, D., Grenier, P., Cabanis, E., Laval-Jeantet, M., 1986. MR imaging of intravoxel incoherent motions: application to diffusion and perfusion in neurologic disorders. *Radiology* 161, 401–407.

- Le Bihan, D., Johansen-Berg, H., 2012. Diffusion MRI at 25: exploring brain tissue structure and function. *Neuroimage* 61, 324–341.
- Lebel, C., Walker, L., Leemans, A., Phillips, L., Beaulieu, C., 2008. Microstructural maturation of the human brain from childhood to adulthood. *Neuroimage* 40, 1044–1055.
- Leemans, A., Jeurissen, B., Sijbers, J., Jones, D.K., 2009. ExploreDTI: A Graphical Toolbox for Processing, Analyzing, and Visualizing Diffusion MR Data, 3537 ed.
- Leemans, A., Jones, D.K., 2009. The B-matrix must be rotated when correcting for subject motion in DTI data. *Magn. Reson. Med.* 61, 1336–1349.
- Leemans, A., Sijbers, J., Verhoye, M., Van der Linden, A., Van, D.D., 2005. Mathematical framework for simulating diffusion tensor MR neural fiber bundles. *Magn. Reson. Med.* 53, 944–953.
- Lundell, H., Nielsen, J.B., Pfitzner, M., Dyrby, T.B., 2011. Distribution of collateral fibers in the monkey cervical spinal cord detected with diffusion-weighted magnetic resonance imaging. *Neuroimage* 56, 923–929.
- McGrath, J., Johnson, K., O'Hanlon, E., Garavan, H., Gallagher, L., Leemans, A., 2013. White Matter and Visuospatial Processing in Autism: A Constrained Spherical Deconvolution Tractography Study. *Autism Res.* <http://dx.doi.org/10.1002/aur.1290> (Electronic publication ahead of print, in press).
- Metzler-Baddeley, C., Hunt, S., Jones, D.K., Leemans, A., Aggleton, J.P., O'Sullivan, M.J., 2012. Temporal association tracts and the breakdown of episodic memory in mild cognitive impairment. *Neurology* 79, 2233–2240.
- Miller, K.L., Stagg, C.J., Douaud, G., Jbabdi, S., Smith, S.M., Behrens, T.E., Jenkinson, M., Chance, S.A., Esiri, M.M., Voets, N.L., Jenkinson, N., Aziz, T.Z., Turner, M.R., Johansen-Berg, H., McNab, J.A., 2011. Diffusion imaging of whole, post-mortem human brains on a clinical MRI scanner. *Neuroimage* 57, 167–181.
- Moseley, M.E., Cohen, Y., Kucharczyk, J., Mintorovitch, J., Asgari, H.S., Wendland, M.F., Tsuruda, J., Norman, D., 1990. Diffusion-weighted MR imaging of anisotropic water diffusion in cat central nervous system. *Radiology* 176, 439–445.
- Parker, G.D., Marshall, D., Rosin, P.L., Drage, N., Richmond, S., Jones, D.K., 2013. A pitfall in the reconstruction of fibre ODFs using spherical deconvolution of diffusion MRI data. *Neuroimage* 65, 433–448.
- Raffelt, D., Tournier, J.D., Rose, S., Ridgway, G.R., Henderson, R., Crozier, S., Salvado, O., Connelly, A., 2012. Apparent Fibre Density: a novel measure for the analysis of diffusion-weighted magnetic resonance images. *Neuroimage* 59, 3976–3994.
- Reijmer, Y.D., Brundel, M., de, B.J., Kappelle, L.J., Leemans, A., Biessels, G.J., 2013a. Microstructural white matter abnormalities and cognitive functioning in type 2 diabetes: a diffusion tensor imaging study. *Diabetes Care* 36, 137–144.
- Reijmer, Y.D., Leemans, A., Brundel, M., Kappelle, L.J., Biessels, G.J., 2013b. Disruption of the cerebral white matter network is related to slowing of information processing speed in patients with type 2 diabetes. *Diabetes* 62, 2112–2115.
- Reijmer, Y.D., Leemans, A., Heringa, S.M., Wielaard, I., Jeurissen, B., Koek, H.L., Biessels, G.J., 2012. Improved sensitivity to cerebral white matter abnormalities in Alzheimer's disease with spherical deconvolution based tractography. *PLoS One* 7, e44074.
- Scholz, J., Klein, M.C., Behrens, T.E., Johansen-Berg, H., 2009. Training induces changes in white-matter architecture. *Nat. Neurosci.* 12, 1370–1371.
- Sijbers, J., den Dekker, A.J., 2004. Maximum likelihood estimation of signal amplitude and noise variance from MR data. *Magn. Reson. Med.* 51, 586–594.
- Tournier, J.D., Calamante, F., Connelly, A., 2007. Robust determination of the fibre orientation distribution in diffusion MRI: non-negativity constrained super-resolved spherical deconvolution. *Neuroimage* 35, 1459–1472.
- Tournier, J.D., Calamante, F., Connelly, A., 2009. How many diffusion gradient directions are required for HARDI. *Proceedings of the 17th Annual Meeting of the ISMRM*, p. 358.
- Tournier, J.D., Calamante, F., Connelly, A., 2013. A robust spherical deconvolution method for the analysis of low SNR or low angular resolution diffusion data. *Proceedings of the 21st Annual Meeting of the ISMRM*, p. 772.
- Tournier, J.D., Calamante, F., Gadian, D.G., Connelly, A., 2004. Direct estimation of the fiber orientation density function from diffusion-weighted MRI data using spherical deconvolution. *Neuroimage* 23, 1176–1185.
- Tournier, J.D., Mori, S., Leemans, A., 2011. Diffusion tensor imaging and beyond. *Magn. Reson. Med.* 65, 1532–1556.
- Tuch, D.S., 2004. Q-ball imaging. *Magn. Reson. Med.* 52, 1358–1372.
- Tuch, D.S., Reese, T.G., Wiegell, M.R., Makris, N., Belliveau, J.W., Wedeen, V.J., 2002. High angular resolution diffusion imaging reveals intravoxel white matter fiber heterogeneity. *Magn. Reson. Med.* 48, 577–582.
- Verhoeven, J.S., Rommel, N., Prodi, E., Leemans, A., Zink, I., Vandewalle, E., Noens, I., Wagemans, J., Steyaert, J., Boets, B., Van de Winckel, A., De, C.P., Lagae, L., Sunaert, S., 2012. Is there a common neuroanatomical substrate of language deficit between autism spectrum disorder and specific language impairment? *Cereb. Cortex* 22, 2263–2271.
- Vos, S.B., Jones, D.K., Jeurissen, B., Viergever, M.A., Leemans, A., 2012. The influence of complex white matter architecture on the mean diffusivity in diffusion tensor MRI of the human brain. *Neuroimage* 59, 2208–2216.
- Wakana, S., Caprihan, A., Panzenboeck, M.M., Fallon, J.H., Perry, M., Gollub, R.L., Hua, K., Zhang, J., Jiang, H., Dubey, P., Blitz, A., van, Z.P., Mori, S., 2007. Reproducibility of quantitative tractography methods applied to cerebral white matter. *Neuroimage* 36, 630–644.
- Wang, H.C., Hsu, J.L., Leemans, A., 2012. Diffusion tensor imaging of vascular Parkinsonism: structural changes in cerebral white matter and the association with clinical severity. *Arch. Neurol.* 1–9.
- Wedeen, V.J., Hagmann, P., Tseng, W.Y., Reese, T.G., Weisskoff, R.M., 2005. Mapping complex tissue architecture with diffusion spectrum magnetic resonance imaging. *Magn. Reson. Med.* 54, 1377–1386.